Supporting Information

Backlund et al. 10.1073/pnas.1216687109

SI Text

Image Formation of an Electric Dipole Emitter. Our simulations model the simplified optical system depicted in Fig. S1, which is similar to systems depicted in refs. 1–3. Specifically, we consider an emitter embedded slightly below the surface of a polymer that is spin-coated on a glass coverslip. In this situation, the objective lens will collect forward propagating light emitted by the dipole in addition to backward propagating light that has been reflected by the air–polymer interface. Because the refractive index mismatch between the polymer and glass is minor ($n_{glass} = 1.518$ vs. $n_{polymer} = 1.49$), we ignore the effects of this interface. After the electric fields at the image plane have been calculated, it is straightforward to augment our simulations to account for polarization, aberrations, and the Double-Helix Point Spread Function (DH-PSF) mask.

Theoretical calculations that extend the pioneering work of Richards and Wolf (4) and predict the image formed by an emitter with a fixed dipole orientation embedded at or near an interface have been developed in the studies by Enderlein (5) and Böhmer and Enderlein (6). In addition, ref. 7 describes methods for simulating a freely rotating emitter or a cluster of tightly packed randomly oriented dipoles (such as a nanoscale fluorescent bead). Furthermore, refs. 8 and 9 describe the impact of subwavelength thin films on dipole emission. Subsequent investigations (10) showed the effects of layered media on the intensity distributions observed at the back focal plane and image plane of a high-N.A. optical system.

Our general strategy will be to decompose the emission pattern of the dipole into a basis of plane waves. The effects of the air–polymer interface and the image-forming optics will be determined for each plane–wave component, and the intensity distribution formed on a camera sensor will then be calculated by integrating over all of the plane–wave contributions that propagate through the imaging system. We begin by considering a dipole emitter embedded a distance z_0 below the surface of an air–polymer interface, with a fixed azimuthal orientation $\phi = \alpha$ and a polar angle of $\theta = \beta$. From ellipsometry measurements, we determined the polymer thickness z_0 to be 30–35 nm. If we consider the plane–wave component of this dipole's emission with propagation direction given by $\hat{k} = \{\sin(\eta)\cos(\psi), \sin(\eta)\sin(\psi), \cos(\eta)\}$, where ψ and η are the azimuthal and polar orientations of the propagation direction, respectively, then the electric field associated with this wave is given by

$$\hat{E}(\eta,\psi) = \hat{e}_s\left[\sin(\beta)\sin(\psi-\alpha)E_s^{\parallel}(\eta)\right] + \hat{e}_p\left[\sin(\beta)\cos(\psi-\alpha)E_p^{\parallel}(\eta) + \cos(\beta)E_p^{\perp}(\eta)\right], \quad \textbf{[S1]}$$

where

$$\begin{aligned} E_s^{\parallel}(\eta) &= -n_{glass}\left[e^{-ikz_0\cos(\eta)} + R_s(\eta)e^{ikz_0\cos(\eta)}\right] \\ E_p^{\parallel}(\eta) &= n_{glass}\cos(\eta)\left[e^{-ikz_0\cos(\eta)} - R_p(\eta)e^{ikz_0\cos(\eta)}\right]. \\ E_p^{\perp}(\eta) &= n_{glass}\sin(\eta)\left[e^{-ikz_0\cos(\eta)} + R_p(\eta)e^{ikz_0\cos(\eta)}\right] \end{aligned} \quad \textbf{[S2]}$$

In the above expressions, $\hat{e}_s = \{-\sin(\psi), \cos(\psi), 0\}$ and $\hat{e}_p = \{\cos(\psi)\cos(\eta), \sin(\psi)\cos(\eta), -\sin(\eta)\}$ are the unit vectors perpendicular to $\hat{k}$, with $\hat{e}_s$ also perpendicular to the optical axis. The superscripts $\parallel$ and $\perp$ denote whether a given component of the E-field is parallel or perpendicular to the interface. The wave number is $k = 2\pi n_{glass}/\lambda$, and $R_s(\eta)$ and $R_p(\eta)$ are the Fresnel reflection coefficients for s and p polarized waves at a polymer–air interface (these terms account for the portion of backward-propagating light reflected at the interface); $\lambda = 609$ nm for DCDHF-N-6 in poly(methyl methacrylate) (11). The effect of the optical imaging system is to map a plane wave with propagation direction $\hat{k}$ to another plane wave with a new propagation direction $\hat{k}' = \{\sin(\eta')\cos(\psi'), \sin(\eta')\sin(\psi'), \cos(\eta')\}$. This mapping is determined by Abbe's sine condition: $M\sin(\eta') = n_{glass}\sin(\eta)$; here, we assume an image formed in air with magnification M. The azimuthal coordinate is unchanged between input and output (i.e., $\psi' = \psi$). Finally, to determine the electric field present at the image plane, all angular contributions to the total field are integrated together. Closed-form expressions exist for the integration over ψ'; however, the integration over η' must be done numerically. The following integral must be evaluated:

$$\begin{bmatrix} E_x(\rho,\phi) \\ E_y(\rho,\phi) \end{bmatrix} = \int_0^{\eta'_{\max}} \sqrt{\frac{\cos(\eta')}{n_{glass}\cos(\eta)}}\, e^{-ikz_1\cos(\eta)}\sin(\eta') \begin{bmatrix} e_x \\ e_y \end{bmatrix} d\eta'. \quad \textbf{[S3]}$$

Note that the image plane has been parameterized using polar coordinates (ρ, φ) and that the polarized components of the electric field are calculated for two orthogonal directions, x and y. In the above expression, the upper bound of integration is set by the maximally inclined plane wave that can be captured by the microscope objective, and it is determined by the objective's numerical aperture ($NA = 1.4$) and magnification ($M = 100$): $\eta'_{\max} = \sin^{-1}(NA/M) = .014$ rad. Furthermore, the amount of defocus is given by z_1. [Focusing beyond the emitter (i.e., moving the objective to the coverslip) corresponds to z_1 of positive sign.] The terms e_x and e_y are given by

$$\begin{aligned} e_x &= \frac{\sin(\beta)}{2}\Big\{J_0\cos(\alpha)\left[\cos(\eta')E_p^{\parallel} - E_s^{\parallel}\right] \\ &\quad - J_2\cos(2\varphi-\alpha)\left[\cos(\eta')E_p^{\parallel} + E_s^{\parallel}\right]\Big\} \\ &\quad - iJ_1\cos(\beta)\cos(\varphi)\cos(\eta')E_p^{\perp} \\ e_y &= \frac{\sin(\beta)}{2}\Big\{J_0\sin(\alpha)\left[\cos(\eta')E_p^{\parallel} - E_s^{\parallel}\right] \\ &\quad - J_2\sin(2\varphi-\alpha)\left[\cos(\eta')E_p^{\parallel} + E_s^{\parallel}\right]\Big\} \\ &\quad - iJ_1\cos(\beta)\sin(\varphi)\cos(\eta')E_p^{\perp}, \end{aligned} \quad \textbf{[S4]}$$

where $J_{0,1,2}$ are Bessel functions of the first kind with the argument $k'\rho\sin(\eta')$, and $k' = \frac{2\pi}{\lambda}$. Similar expressions exist for the magnetic fields. However, we assume that, for all of the propagation media, $\mu_r = 1$. For nonpolarization sensitive detection, the intensity distribution at the image plane may be calculated as

$$I(\rho,\varphi) = \frac{c\varepsilon_0}{2}\left[E_x(\rho,\varphi)E_x^*(\rho,\varphi) + E_y(\rho,\varphi)E_y^*(\rho,\varphi)\right]. \quad \textbf{[S5]}$$

Practically, the integral in Eq. **S3** was computed using a rectangular approximation by substituting Eq. **S2** into Eq. **S4** and then evaluating the integrand at a fixed location (ρ, φ) while varying η' from zero to η'_{max}. Summing the results together yields the electric fields at the single point in the image plane (ρ, φ). In our simulations, $E_x(\rho, \varphi)$ and $E_y(\rho, \varphi)$ were evaluated within a 256 × 256 grid, with samples spaced a distance of 1 μm apart. (After accounting for the magnification factor of 100, the effective spacing at the focal plane is 10 nm.) Also, for each location within the image plane, the integrand was evaluated for 100 different values of η' spaced evenly between zero and η'_{max} (i.e., $\delta\eta' = .01 \times \sin^{-1}(1.4/100) = .00014$ rad). Performing this calculation for an entire 256 × 256 region takes approximately 2 min running 32-bit MATLAB on a standard office desktop computer (Dell Optiplex 960 with a 3 GHz Intel Core 2 Duo CPU).

Equipped with a theoretical model describing the image formed by a dipole emitter, we may begin to make modifications to account for the particulars of our optical design. Because a polarizing beam splitter was used to record two orthogonal polarizations of the electric field in separate regions of an image sensor, the two polarized intensity distributions [$I_x(\rho, \varphi)$ and $I_y(\rho, \varphi)$] are calculated as

$$\begin{bmatrix} I_x(\rho,\varphi) \\ I_y(\rho,\varphi) \end{bmatrix} = \frac{c\varepsilon_0}{2} \begin{bmatrix} E_x\left(\rho,\varphi\right)E_x^*\left(\rho,\varphi\right) \\ E_y\left(\rho,\varphi\right)E_y^*\left(\rho,\varphi\right) \end{bmatrix}. \qquad \textbf{[S6]}$$

Furthermore, the geometry of our setup causes light reflected by the beam splitter to incur one additional reflection as it propagates through the imaging pathway. Therefore, simulated images for one polarization must be reflected about the $\varphi = 90°$ axis before comparison with acquired data. (Here, the *x* and *y* polarized simulations can be related to the *T* and *R* channels, respectively, by taking into account the appropriate reflections and rotations introduced by the experimental setup. Fig. 1*B* depicts the specific geometrical transformations that each polarized image undergoes before it is projected onto the image sensor.)

Modeling Dipole Emission Effects on the DH-PSF. To simulate how a dipole emitter undergoes phase modulation to form the DH-PSF, we use the same framework described above and numerically integrate Eq. **S3**. The electric fields were sampled with a different pixel size and number of samples from above to match the discrete pixels of the DH-PSF phase mask and avoid ringing artifacts of the discrete Fourier transform (1,024 × 1,024 pixels, 5.95-μm pixel size in the image plane, 59.5-nm pixel size in the focal plane). The resulting electric fields at the image plane are calculated as

$$\begin{aligned} E_x^{DH-PSF}\left(\rho,\varphi\right) &= FT\left\{FT\{E_x(\rho,\varphi)\}e^{i\psi^{DH-PSF}\left(\rho',\varphi'\right)}\right\} \\ E_y^{DH-PSF}\left(\rho,\varphi\right) &= FT\left\{FT\{E_y(\rho,\varphi)\}e^{i\psi^{DH-PSF}\left(\rho',\varphi'\right)}\right\} \end{aligned}. \qquad \textbf{[S7]}$$

In the above equation, $FT\{\}$ denotes the Fourier transform operation, whereas two cascaded Fourier transforms model the image formation process of a 4*f* optical system (12). The function $\psi^{DH\text{-}PSF}(\rho',\varphi')$ models the phase delay imparted by the DH-PSF pattern programmed into the spatial light modulator (SLM). In this simulation, the mask is oriented such that its discontinuities are along the *x* axis; therefore, the *x* polarization has parallel-type behavior, whereas the *y* polarization has perpendicular-type behavior. It is convenient to normalize the radial coordinate, ρ', such that the electric field is zero at distances greater than $\rho' = 1$ from the center of the pupil. (If one were to use nonnormalized coordinates, $\rho' = 1$ corresponds to the distance $f\ NA/M$ from the center of the aperture, where *f* is the focal length of the optical system.) Simulated polarized images of the DH-PSF (Fig. S2 *A* and *B*), expressed as $I_x^{DH-PSF} \propto |E_x^{DH-PSF}|^2$ and $I_y^{DH-PSF} \propto |E_y^{DH-PSF}|^2$, were then fit by our double Gaussian estimator to map out the response of DH-PSF as a function of dipole orientation (θ, ϕ). The double Gaussian estimator finds the best-fitting parameters $(A_{L1,L2}, x_{L1,L2}, y_{L1,L2}, \sigma_{L1,L2})$ that minimize the summed square error between the function

$$\begin{aligned} I^{\mathrm{DG}}(\rho,\varphi) = {} & A_{L1}\exp\left[\frac{-(\rho\cos\varphi - x_{L1})^2 - (\rho\sin\varphi - \mathrm{y}_{L1})^2}{2{\sigma_{L1}}^2}\right] \\ & + A_{L2}\exp\left[\frac{-(\rho\cos\varphi - x_{L2})^2 - (\rho\sin\varphi - \mathrm{y}_{L2})^2}{2{\sigma_{L2}}^2}\right] \end{aligned} \qquad \textbf{[S8]}$$

and the simulated DH-PSF images $I_x^{DH\text{-}PSF}$ and $I_y^{DH\text{-}PSF}$ using the optimization function lsqnonlin. $(A_{L1,L2}, x_{L1,L2}, y_{L1,L2}, \sigma_{L1,L2})$ are the fitted amplitudes, *x* position, *y* position, and widths (SD), respectively, of each Gaussian lobe of the DH-PSF. The double Gaussian estimator produced reasonable fits of the DH-PSF for most dipole orientations (Fig. S2 *C* and *D*). The spatio-orientation space (z, θ, ϕ) was sampled at a rate of ($\delta z = 50$ nm, $\delta\theta \cong 6.5°$, $\delta\phi \cong 6.5°$), which is shown as black dots in Fig. S2*E*, column 1. Observable parameters of the DH-PSF for orientation fitting were then calculated from the double Gaussian fit parameters using the relations

$$LD(z,\theta,\phi) = \frac{N_x - N_y}{N_x + N_y}, \qquad \textbf{[S9]}$$

$$LA(z,\theta,\phi) = \frac{A_{L1} - A_{L2}}{A_{L1} + A_{L2}}, \qquad \textbf{[S10]}$$

$$\Delta x(z,\theta,\phi) = \frac{x_{L1} + x_{L2}}{2}, \qquad \textbf{[S11]}$$

and

$$\Delta y(z,\theta,\phi) = \frac{y_{L1} + y_{L2}}{2}, \qquad \textbf{[S12]}$$

where N_x and N_y are the total number of photons in the *x* and *y* polarization channels, respectively. Linear dichroism *LD* was found to have essentially no dependence on emitter defocus *z* (Fig. 2*B*), but lobe asymmetry *LA* (Fig. S2 *E* and *F*) and lateral shifts $(\Delta x, \Delta y)$ (Fig. S2 *G*–*J*) have diverse behavior across (z, θ, ϕ). Notably, it is the contrasting behavior between *LA* in the *x* and *y* channels [termed the parallel (Fig. S2*E*) and perpendicular (Fig. S2*F*) behaviors in the text] that breaks the degeneracy of *LD* and enables effective measurement of orientation with the DH-PSF.

Modeling and Correction of Optical Aberrations. Our objective lens and relay optics induced a slight amount of spherical aberration in the images recorded on the electron-multiplying charge-coupled device (EMCCD) camera. Simulations of the standard PSF were augmented accordingly by applying a spherical aberration phase mask to the electric field that we calculated to be present at the pupil (aperture) plane of our microscope. We found the aberrated electric fields for *x* and *y* polarizations simply by taking the Fourier transform of the unaberrated fields present at the image plane, multiplying by the appropriate phase mask, and then inverse Fourier transforming:

$$\begin{aligned} E_x^{Sph.Ab.}(\rho,\varphi) &= IFT\left\{FT\{E_x(\rho,\varphi)\}e^{i\psi^{Sph.Ab,}\left(\rho',\varphi'\right)}\right\} \\ E_y^{Sph.Ab.}(\rho,\varphi) &= IFT\left\{FT\left\{E_y\left(\rho,\varphi\right)\right\}e^{i\psi^{Sph.Ab.}\left(\rho',\varphi'\right)}\right\} \end{aligned}. \qquad \textbf{[S13]}$$

$IFT\{\}$ denotes the inverse Fourier transform operation. The aberration function $\psi^{Sph.Ab.}(\rho', \varphi')$ models the phase delay effects of spherical aberration. Using the ρ' coordinate system, first-order spherical aberration is given explicitly by the polynomial (13)

$$\psi^{Sph\,Ab.}(\rho',\phi') = A\left(6\rho'^4 - 6\rho'^2 + 1\right). \qquad \textbf{[S14]}$$

The coefficient A sets the magnitude of aberration present in the system. We determined this coefficient heuristically. Interestingly, the incorporation of spherical aberration into the simulated images only improved matches with the clear-aperture defocused PSFs, and therefore, it was only included there. Accounting for spherical aberration did not improve matches to simulated DH-PSF images and therefore, was omitted for this part of the analysis.

The clear-aperture defocused PSFs also exhibited elements of astigmatism and comatic aberration. Instead of incorporating these effects in simulation, we corrected these distortions experimentally using the same SLM that was used to create the DH-PSF. Because coma and astigmatism are inherently asymmetric and lead to more dramatic distortions in the defocused PSF, we found it more expedient to experimentally diagnose and remove these aberrations. In-house software was developed for loading coma and astigmatism phase masks onto the SLM and adjusting the magnitude of their aberration coefficients. We used phase masks of the form

$$\begin{aligned}\psi^{Coma}(\rho',\varphi') &= B\left(3\rho'^3 - 2\rho'\right)\cos\left(\varphi' - \varphi^{Coma}\right)\\ \psi^{Astig.}(\rho',\varphi') &= C\left\{6\rho'^2\cos\left[2\left(\varphi' - \varphi^{Astig.}\right)\right]\right\}\end{aligned}. \qquad \textbf{[S15]}$$

To find optimal values for the parameters B, C, φ^{Coma}, and $\varphi^{Astig.}$, data from our EMCCD was displayed in real time, and the SLM driving software was used to modify the aberration coefficients to minimize irregularities in the PSF. Because of the unique geometry of our optical setup, the SLM appears to have different orientations when viewed in each polarization channel. Furthermore, the imaging pathways for the two different polarizations induced slightly different aberrations. Therefore, it was necessary to image the x and y polarized images of defocused molecules sequentially, with different phase masks loaded onto the SLM to correct the aberrations present in each of the separate imaging paths. When recording DH-PSF data, we observed that the 3D PSFs were more robust to the effects of minor aberrations, and no experimental corrections were required.

Single-Molecule Orientation and 3D Position Estimation with the DH-PSF. As discussed in *Materials and Methods*, ($x_{apparent}$, $y_{apparent}$, z, LA, LD) was measured for each single molecule (SM) in each detection channel (red, gold, green, and blue in the text) by fitting SM DH-PSF images with a double Gaussian estimator. This estimator is identical to the one used for the simulated DH-PSF response and is detailed above. SM orientation and position measurements were completed in two steps. First, orientation was estimated using the measured z position, lobe asymmetry, and linear dichroism across the four detection channels. Next, given this orientation, the calculated (Δx, Δy) shift from simulations was subtracted from ($x_{apparent}$, $y_{apparent}$) to yield the true lateral position of the SMs.

The orientation measurement process was carried out as follows. Calibrated measurements of (z, LA, LD) from each channel were grouped together such that their measured z positions were within 50 nm of each other. (Channels with a double Gaussian fit that failed because of severe lobe asymmetry had their lobe asymmetry measured by hand-designating each Gaussian spot of the DH-PSF and fitting it to a 2D Gaussian function). The measurements ($z_{meas,i}$, $LA_{meas,i}$, $LD_{meas,i}$) from all channels i were input to the orientation-fitting algorithm, which used the MATLAB function lsqnonlin to find the orientation (θ, ϕ) that minimizes

$$\begin{aligned}\sum_{i=1}^{4}\Big\{ & w\left(LA_{sim}(z_i,\theta,\phi)\right)\left[LA_{meas,i} - LA_{sim}(z_i,\theta,\phi)\right]^2\\ & + \left[LD_{meas,i} - LD_{sim}(z_i,\theta,\phi)\right]^2\Big\},\end{aligned} \qquad \textbf{[S16]}$$

the weighted squared difference between measurements and simulations of LA and LD, where the index i refers to measurements from each of the four channels,

$$w(x) = \begin{cases} 1, & |x| < 2/3 \\ 3(1-|x|), & |x| \geq 2/3 \end{cases}, \qquad \textbf{[S17]}$$

the subscripts *meas* and *sim* refer to experimental and theoretical values, respectively, and $z_i = z_{meas,i} + z_{offset,i}$ is a calibrated z position that compensates for relative defocus between polarization channels of the 4f system. The piecewise linear-weighting function $w(x)$ serves to deemphasize simulated values of LA that are difficult to measure because of low signal-to-noise ratio (i.e., LA is deemphasized when $|LA| > 2/3$). Explicitly, $LD_{meas,i}$ is calculated from pairs of channels such that

$$LD_{red} = LD_{green} = \frac{N_{red} - N_{green}}{N_{red} + N_{green}} \qquad \textbf{[S18]}$$

and

$$LD_{gold} = LD_{blue} = \frac{N_{gold} - N_{blue}}{N_{gold} + N_{blue}}. \qquad \textbf{[S19]}$$

Finally, $z_{offset,i}$ is calibrated for each measured SM by finding the best value that allows measurements of LA to overlap with calculated values of LA for the entire z scan. Because of local sample tilt, this value is slightly different for each SM that we measured. For molecule 1, z_{offset} = 70 nm for the transmitted polarization channels, and z_{offset} = 200 nm for the reflected polarization channels. For molecule 2, z_{offset} = 0 nm for the transmitted polarization channels, and z_{offset} = −200 nm for the reflected polarization channels. For molecule 3, $z_{offset,T}$ = 186 nm, and $z_{offset,R}$ = −185 nm. For molecules 4, 5, and 6, $z_{offset,T} = z_{offset,R}$ = 0 nm. For positions and orientations (z_i, θ, ϕ) where simulations were not explicitly carried out, the MATLAB interpolation function TriScatteredInterp was used to evaluate $LA_{sim}(z_i, \theta, \phi)$ and $LD_{sim}(z_i, \theta, \phi)$. The above orientation estimator is a first-order approach that matches experimental data to a library of simulated data to measure orientation; more sophisticated optimization functions or finer sampling of simulated data may improve orientation-fitting performance.

When matching experimental measurements of (z, LA, LD) to simulations, care must be taken in ensuring that ϕ is transformed appropriately considering the optical system and orientation of the DH-PSF mask. Mapping ϕ_{IIP} in the intermediate image plane (IIP) (Fig. 1*B*) to a specific orientation relative to the DH-PSF mask (ϕ_{mask}), we obtain the following relations:

$$\begin{aligned}\phi_{red,mask} &= \phi_{IIP}\\ \phi_{gold,mask} &= \phi_{IIP} + \pi/2\\ \phi_{green,mask} &= 3\pi/2 - \phi_{IIP}\\ \phi_{blue,mask} &= -\phi_{IIP}\end{aligned}. \qquad \textbf{[S20]}$$

Furthermore, the red and green channels show parallel-type behavior (Fig. 1*B Inset*) because their polarization is parallel to the phase discontinuities of the DH-PSF mask, whereas the gold and blue channels show perpendicular-type behavior.

Two strategies for calculating the true lateral position of each SM were used. The first strategy uses measurements of ($z_{meas,i}$, $LA_{meas,i}$, $LD_{meas,i}$) at a single z position from all four channels i to measure orientation (θ, ϕ). Then, the calculated [$\Delta x_i(z_i, \theta, \phi)$, $\Delta y_i(z_i, \theta, \phi)$] shift from simulations is subtracted from the apparent position ($x_{apparent,i}$, $y_{apparent,i}$) for each channel to recover the true location of the molecule. The second strategy involves averaging all such pointwise measurements of orientation over the entire z scan to yield $(\overline{\theta}, \overline{\phi})$. Then, the calculated shift $[\Delta x_i(z_i, \overline{\theta}, \overline{\phi;}), \Delta y_i(z_i, \overline{\theta}, \overline{\phi})]$ for this single orientation $(\overline{\theta}, \overline{\phi})$ is used to correct the lateral position of the SM. This approach has the benefit of reducing orientation measurement noise at the cost of requiring multiple snapshots of each SM. Again, the MATLAB interpolation function TriScatteredInterp was used to evaluate [$\Delta x_i(z_i, \theta, \phi)$, $\Delta y_i(z_i, \theta, \phi)$].

Clear-Aperture Defocused Image Template Matching. By matching simulations to the image of a defocused molecule (without the DH-PSF), a well-established SM orientation determination method, we gain an independent estimate of that molecule's dipole orientation. This information is used for verification of our DH-PSF–based orientation estimation algorithms. Data were compared with a list of simulated templates. The dipole orientation of a defocused molecule was then estimated as the orientation of the template that yielded the closest fit to the actual data.

Using the simulation methods described above, a list of templates was generated for both the x and y polarized images of a defocused molecule. This template list included dipole emitters simulated at all orientations of θ from 0° to 90° and ϕ from 0° to 355° spaced at intervals of 5°. Hence, 1,368 pairs of polarized intensity distributions were simulated. In practice, all dipole emission patterns were calculated using MATLAB. Spherical aberration was simulated by first calculating the unaberrated high-resolution electric fields of an emitter with fixed orientation at the image plane. The result was zero-padded to ensure adequate sampling in the Fourier domain, and then, it was discrete Fourier-transformed using MATLAB's fft2 function. The appropriate phase masks were applied as described above, and then, an inverse Fourier transform was applied using MATLAB's ifft2 function to recover the aberrated image. By visually comparing simulations with acquired data, we found that the spherical aberration coefficient $A = 1.8$ yielded simulated images that closely matched experiment (Eq. **S14**). Furthermore, by comparing simulation with experiment, we estimated the defocus to be 1 ± 0.15 μm below the emitter. (For a given field of view, the precise defocus depth was estimated by eye to generate a set of templates). To account for the pixelation effects of the EMCCD, simulations were performed on a high-resolution discretization of the image plane (256 × 256-μm extent with 1 × 1-μm sampling, which is equivalent to 2.56 × 2.56 μm with 10 × 10-nm pixels in object space). Subdivisions were made in the high-resolution grid (16 × 16 μm corresponding to 160 × 160 nm in object space), and intensity values within each subdivision were summed together. This summation leads to 16 × 16-pixel templates that match the actual pixel size of our EMCCD. Each pair of polarized images was then normalized by the sum of the squares of its pixel values [that is, if I_x^j and I_y^j denote the x and y polarized images corresponding with the jth template in our list, the normalized templates are calculated as

$$\left.\begin{aligned} \tilde{I}_x^j &= \frac{I_x^j}{\sqrt{\sum\limits_{m=1}^{M}\sum\limits_{n=1}^{M}\left(I_x^j[m,n]\right)^2+\left(I_y^j[m,n]\right)^2}} \\ \tilde{I}_y^j &= \frac{I_y^j}{\sqrt{\sum\limits_{m=1}^{M}\sum\limits_{n=1}^{M}\left(I_x^j[m,n]\right)^2+\left(I_y^j[m,n]\right)^2}} \end{aligned}\right]. \qquad \textbf{[S21]}$$

The additional brackets are used to denote the [m,n]th pixel in an image, and M is the total number of pixels along a given dimension in the template (in this case, $M = 16$).

The normalized template that most closely matched the defocused images was determined as follows. A 16 × 16 region of interest was drawn around the image made by both the x and y polarized intensities (T and R channels, respectively, of Fig. 1*B*) of an SM. Background intensity was estimated by calculating the mean number of photons per pixel detected in a manually selected rectangle of ∼20 × 20 to 40 × 40 pixels nearby the molecule of interest and subsequently subtracted from each pixel in the region of interest containing the single defocused molecule. The cross-correlation between each of the two background-subtracted polarized images, D_x and D_y, and each template of generated images was then computed. The maximum values of the two resulting cross-correlation matrices were summed together, and the result, C_j, was stored. Mathematically, we evaluated

$$\begin{aligned} C_j = \max\nolimits_{p,q}&\left(\sum_{m=1}^{M}\sum_{n=1}^{M} D_x[m,n]\tilde{I}_x^j[m+p,n+q]\right) \\ &+ \max\nolimits_{p,q}\left(\sum_{m=1}^{M}\sum_{n=1}^{M} D_y[m,n]\tilde{I}_y^j[m+p,n+q]\right). \end{aligned} \qquad \textbf{[S22]}$$

This operation can be performed efficiently using MATLAB's xcorr2 function. After C_j was computed for the entire template list, the template yielding the largest value of C_j was chosen as the best match, and the dipole orientation of that template was used as an estimate of the dipole orientation of the data. Fig. S3 shows the results of using template matching to estimate dipole orientation for the two molecules examined in the text. Representative image acquisitions are plotted with the simulated images of the templates that yield the best match. For both molecules, a defocus of $z_1 = 1.13$ μm was used to generate a list of templates. To benchmark the precision of this technique, orientation was estimated repeatedly for the same molecule using data from successive acquisitions. The mean orientation estimates and SDs in θ and ϕ were calculated (*Results and Discussion*).

Cramer–Rao Lower Bound for the Polarization-Sensitive DH System. In the text, we presented the polarization-sensitive DH microscope as a means to simultaneously measure 3D position and orientation of an SM. Here, we quantitatively compare this approach with established methods that use a clear-aperture standard PSF system (1, 7). We calculate the photon-limited precision that can be achieved in estimating the position and orientation of a dipole using the Cramer–Rao Lower Bound (CRLB) (14).

The CRLB is defined as the inverse of the Fisher Information (FI) matrix, which assesses the information contained in a probability distribution for estimation of parameters. The FI matrix is additive; therefore, for a multiple channel system, the FI matrix of each channel is summed to get the total FI and then inverted to get the CRLB. The lower bound SD (σ_{LB}), which is the square root of the CRLB, directly yields a lower bound for the precision of an unbiased estimator in the same units as the measured data.

Thus, for the five-parameter estimation problem, the σ matrix is a 5 × 5 matrix. For 3D imaging and localization, we are interested in the minimum localization volume. One measure of this uncertainty volume is

$$\sigma_{3D} = \frac{4\pi}{3}\sigma_x \cdot \sigma_y \cdot \sigma_z. \qquad \textbf{[S23]}$$

For the CRLB simulation, the dipole is assumed to be immersed in a medium of index 1.52 (no interface) and emitting at $\lambda = 610$ nm. The objective lens has an N.A. of 1.4. The pixel size is 160 nm in the object plane. We assume the imaging system to be shift-invariant, which is a good approximation in the central region of the field of view. The number of photons collected by the objective lens depends on the dipole's polar orientation. CRLB calculations show that most photons are collected when the dipole is oriented along $\theta = 90°$, and thus, for photon-limited systems, all images are normalized according to this case (same number of photons emitted). The total number of photons detected for the dipole along $\theta = 90°$ is taken to be 5,000, and all calculations are performed in the shot noise limit. In all calculations, the number of photons detected in the standard system is the same as the number in the DH system properly divided among the four channels.

Fig. S6*A* shows the localization and orientation error lower bound as a function of θ with and without background. The amount of defocus for either system is chosen to optimize the precision based on the lowest CRLB. Thus, the axial defocus for the standard (clear aperture) system is $z = 100$ nm, whereas the DH system performs best at focus ($z = 0$). Our calculations also show that σ_{3D}, σ_θ, and σ_ϕ are relatively constant as a function of the polar angle θ. To make a fair comparison, we choose $\phi = 45°$ in Fig. S6*A* to evenly distribute the light between the two linear polarization channels.

The lower bound of the error for angle estimation and 3D position using the four-channel polarization-sensitive DH system is substantially lower than the lower bound of the standard PSF case. As expected, with the inclusion of background, the localization precision of the DH worsens, but it still performs better than the standard case for intermediate θ. The standard system performance is calculated for the optimal defocus, and therefore, it will substantially deteriorate with variations in z. On the contrary, the DH system has a slower variation with defocus and hence, provides a relatively uniform performance with defocus. The lower bound for estimating the angle and position as a function of defocus is shown in Fig. S6 *B* and *C*. The dipole is oriented along a representative direction $(\theta, \phi) = (45°, 45°)$ in Fig. S6*B* and $(\theta, \phi) = (90°, 90°)$ in Fig. S6*C*. It can be seen that the DH system performs better than the standard system over most of the defocus range with and without background.

Calibrations. The behavior of the DH-PSF vs. z was calibrated using a fiducial fluorescent bead. Each field of view was chosen such that it included at least one fiducial bead near the edge of the field. Laser power was kept sufficiently low such that the bead did not bleach appreciably during the experiment, which would otherwise make its emission increasingly anisotropic. *LD* of the beads was found to be ∼0 ± 0.1, justifying its use as an isotropic emitter. The microscope objective was then scanned in z as described in *Materials and Methods*. The angle made by the two lobes of the DH-PSF image of the bead at each z step was recorded to produce an angle vs. z calibration curve to be applied to the fit SMs (Fig. S7*A*), where $z = 0$ was assigned to 0°. Although the simulated DH-PSF of an isotropic point emitter does not translate in (x, y) as a function of z, factors such as sample tilt, aberrations, and imperfect mask alignment produce a baseline shift that must also be calibrated out of SM localizations to recover the true dipole-induced shifts (Fig. S7 *B* and *C*). Because some of the factors that contribute to these calibration curves are different in each of the four mask orientation/polarization channel combinations, we used unique calibration curves for each channel (red, gold, green, and blue in the text).

Sample drift is another experimental effect that could potentially swamp the dipole-induced shifts that we sought to measure. By measuring a separate bead-based calibration curve for each individual z scan of each field of view, we mitigated this potential source of error. In this way, any (x, y) drift occurring during a scan was included in the (x, y) vs. z calibration. We measured multiple reproducible (x, y) shifts across all of our SM z scans, suggesting that drift was effectively removed.

The nanoscale behavior of the DH-PSF is subtly affected by the medium surrounding the SMs and fluorescent beads. As explained in *Materials and Methods*, sample constraints precluded the ability to embed the beads in the same medium as the SMs. Consequently, we measured nonzero residual (x, y) shifts for SMs with θ near 90° (we expect these shifts to be constant), even after applying the bead-based calibrations explained above. To calibrate and remove this residual shift, we chose two molecules with predicted shifts that were fairly constant measured experimentally to have polar orientations θ of ∼80° and ∼85°. Calibration molecule 1 gave good signal in the reflected polarization channel, and therefore, we used the deviation between its measured (x, y) shifts and its predicted shifts to correct all SM shifts in the perpendicular/reflected (blue) and parallel/reflected (green) channels. Calibration molecule 2 gave good signal in the transmitted polarization channel, and therefore, it was used equivalently for the perpendicular/transmitted (gold) and parallel/transmitted (red) channels. We then applied third–eighth-order polynomial fits (chosen by using the lowest order that reproduced the major features as judged by eye) to these residual curves, effectively smoothing them. In cases where the curves needed to be extrapolated to span a full 2-μm depth of field, the smoothed curves were extended with a linear or low-order polynomial that gave the most qualitatively reasonable extrapolation. The measured residual shifts and their piecewise polynomial fits are displayed in Fig. S7 *D* and *E*. These curves were subtracted from the measured shifts of all molecules in the appropriate channels.

1. Patra D, Gregor I, Enderlein J (2004) Image analysis of defocused single-molecule images for three-dimensional molecule orientation studies. *J Phys Chem A* 108(33):6836–6841.
2. Toprak E, et al. (2006) Defocused orientation and position imaging (DOPI) of myosin V. *Proc Natl Acad Sci USA* 103(17):6495–6499.
3. Enderlein J, Toprak E, Selvin PR (2006) Polarization effect on position accuracy of fluorophore localization. *Opt Express* 14(18):8111–8120.
4. Richards B, Wolf E (1959) Electromagnetic diffraction in optical systems. II. structure of the image field in an aplanatic system. *Proc R Soc Lond A Math Phys Sci* 253(1274):358–379.
5. Enderlein J (2000) Theoretical study of detection of a dipole emitter through an objective with high numerical aperture. *Opt Lett* 25(9):634–636.
6. Böhmer M, Enderlein J (2003) Orientation imaging of single molecules by wide-field epifluorescence microscopy. *J Opt Soc Am B* 20(3):554–559.
7. Mortensen KI, Churchman LS, Spudich JA, Flyvbjerg H (2010) Optimized localization analysis for single-molecule tracking and super-resolution microscopy. *Nat Methods* 7(5):377–381.
8. Lukosz W (1981) Light emission by multipole sources in thin layers. I. radiation patterns of electric and magnetic dipoles. *J Opt Soc Am* 71(6):744–754.
9. Hellen EH, Axelrod D (1987) Fluorescence emission at dielectric and metal-film interfaces. *J Opt Soc Am B* 4(3):337–350.
10. Axelrod D (2012) Fluorescence excitation and imaging of single molecules near dielectric-coated and bare surfaces: A theoretical study. *J Microsc* 247(2):147–160.
11. Lord SJ, et al. (2007) Photophysical properties of acene DCDHF fluorophores: Long-wavelength single-molecule emitters designed for cellular imaging. *J Phys Chem A* 111(37):8934–8941.
12. Goodman JW (2005) *Introduction to Fourier Optics* (Roberts & Company, Greenwood Village, CO).
13. Mahajan VN (2007) *Optical Shop Testing*, ed Malacara D (Wiley, New York), pp 498–546.
14. Kay SM (1993) *Fundamentals of Statistical Signal Processing: Estimation Theory* (Prentice Hall, Englewood Cliffs, NJ).

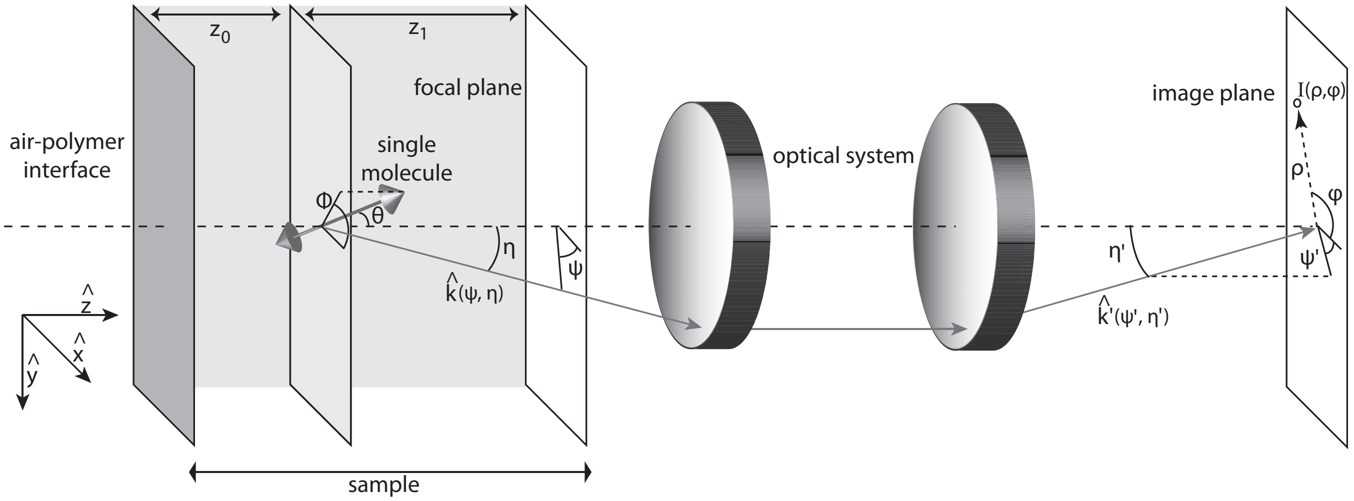

Fig. S1. The simplified imaging system modeled by our simulations. An SM is laterally located along the optical axis, embedded a distance z_0 beneath the surface of a polymer, and positioned z_1 above the focal plane with respect to the optical system. The dipole orientation of the molecule is defined by the polar and azimuthal angles θ and ϕ, respectively. The light that propagates through the optical system can be expressed as a sum of plane waves with wave vector $\hat{k}(\psi, \eta)$, where ψ and η are the azimuthal and polar orientations of the propagation direction, respectively. Our simulations determine how a given input $\hat{k}(\psi, \eta)$ is mapped to a different plane wave $\hat{k}'(\psi', \eta')$ at the output of the optical system. The resulting intensity distribution $I(\rho, \varphi)$ at a given point in the image plane (parameterized using polar coordinates) is then determined by integrating the contributions of each output plane wave component.

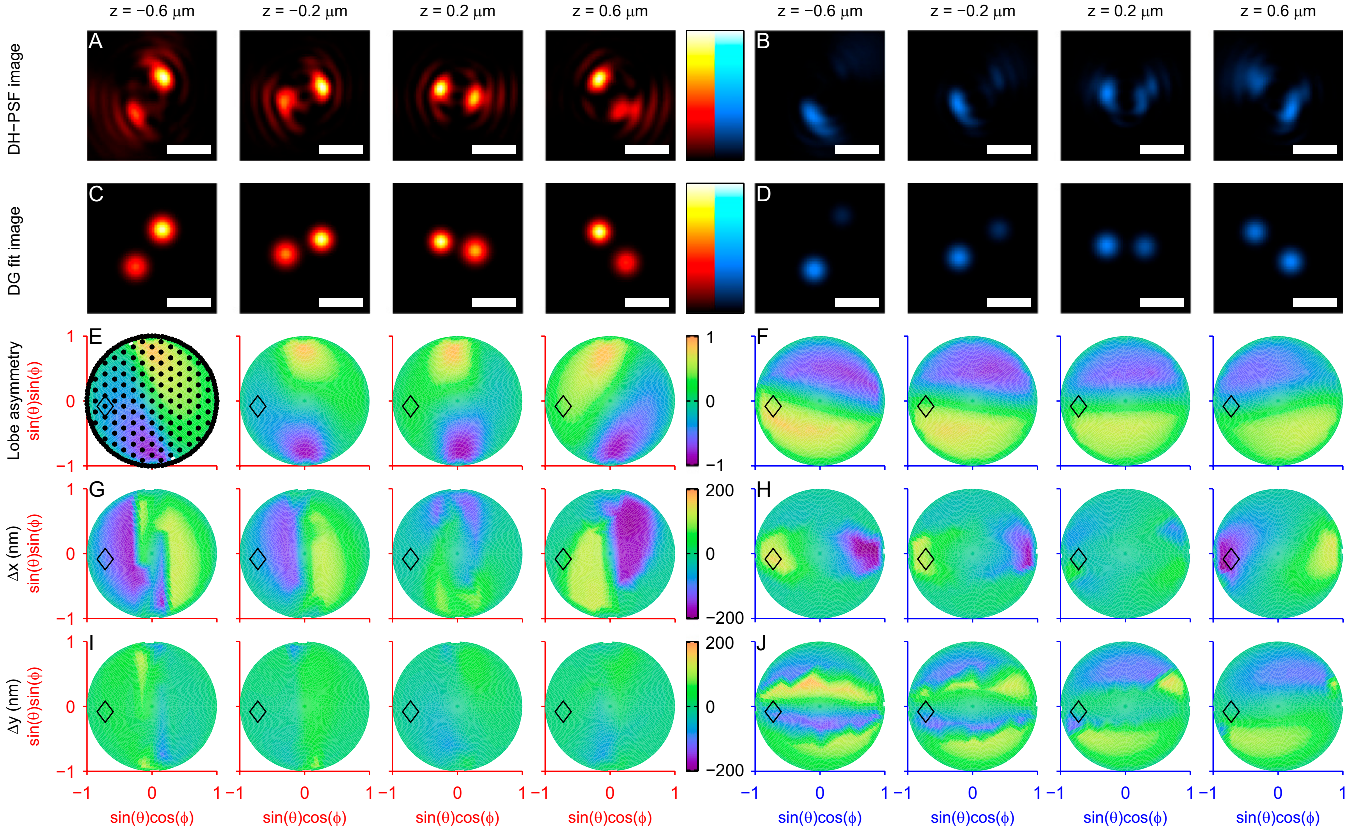

Fig. S2. DH-PSF response to SM orientation and axial position. Simulated DH-PSF images of an SM with orientation $(\theta, \phi) = (47°, -173°)$ at several z positions (each column) in the (*A*) x (parallel) polarization channel (red) and (*B*) y (perpendicular) polarization channel (blue). (*C* and *D*) Images of double Gaussian fits of the DH-PSF images in *A* and *B*, respectively. (*E* and *F*) DH-PSF lobe asymmetry behavior as measured by the double Gaussian estimator as a function of orientation in the two polarization channels. Orientation space is plotted as a 2D map, with horizontal coordinates given by sin(θ)cos(ϕ) and vertical coordinates given by sin(θ)sin(ϕ). Black dots in *E* show the various SM orientations that were simulated to build the library of DH-PSF behaviors; (*G* and *H*) x shift of the DH-PSF in the two polarization channels resulting from the dipole emission pattern, and (*I* and *J*) y shift of the DH-PSF in the two polarization channels. In *E*–*J*, ◇ denotes the orientation $(\theta, \phi) = (47°, -173°)$. (Scale bars: 1 μm.)

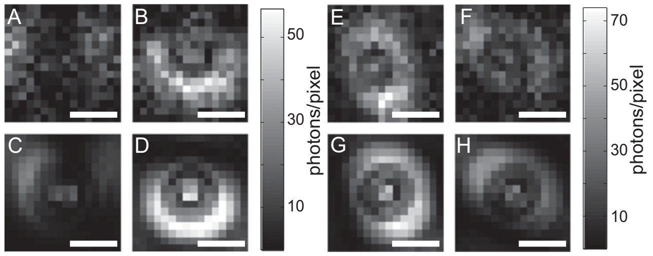

Fig. S3. Determining orientation from defocused images. *A* and *B* show representative acquisitions of molecule 1 in the *T* and *R* channels, respectively. *C* and *D* show the most closely matching set of polarized templates. *E* and *F* show *T* and *R* channel images of molecule 2, whereas *G* and *H* depict the best templates. For these two molecules, a defocus of z_1 = 1.13 μm was used to generate a set of templates. For molecule 1, the mean orientation fit and SD were based on 72 separate 1-s acquisitions. For molecule 2, 27 acquisitions were collected before photobleaching. (Scale bars: 1 μm.)

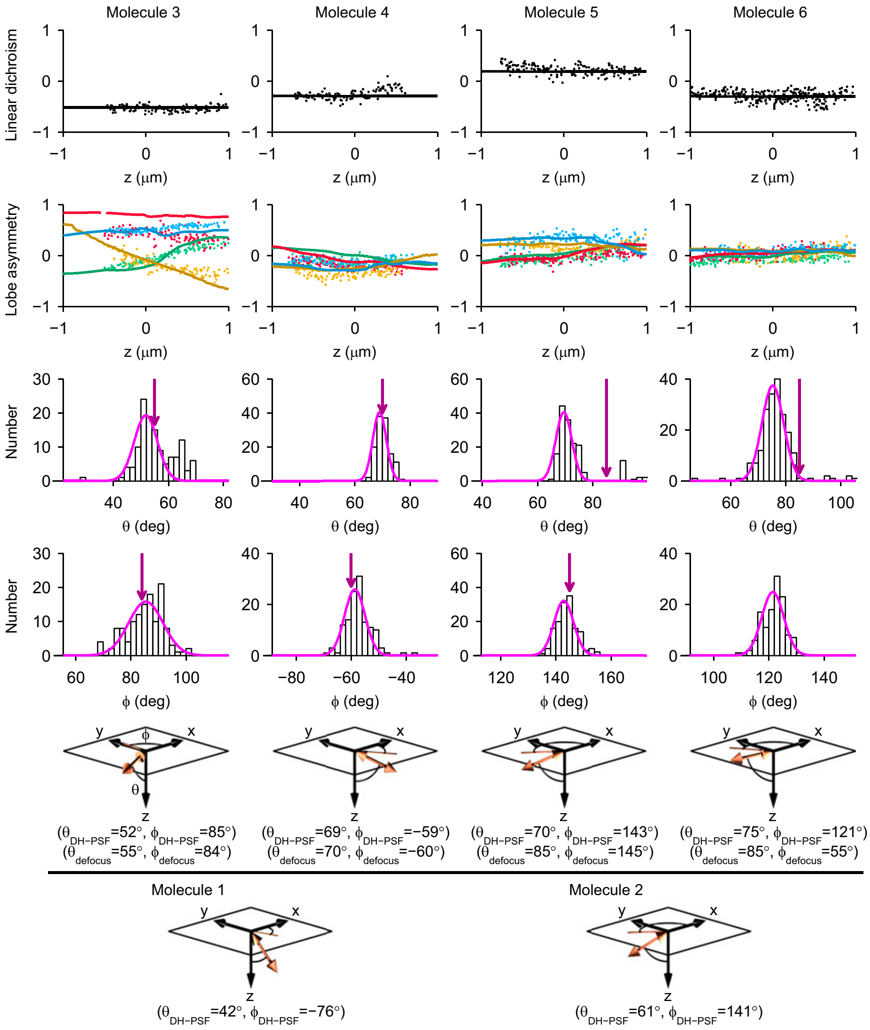

Fig. S4. Orientation estimations of additional molecules. In the top two rows, each measurement of *LD* and *LA* (scatter points) along with the predicted *LD* and *LA* (solid curve) based on the mean fit orientation of each molecule is shown. In the middle two rows, histograms of DH-PSF–based orientation estimations are overlaid with a Gaussian fit (magenta curve). Defocused clear-aperture estimates of orientation are denoted by purple arrows. In the bottom two rows, molecular orientation diagrams depict the measured orientations of molecules 3–6 as well as the orientations of molecules 1 and 2 from the text for comparison. Both molecules 3 and 4 have intermediate inclination, $\theta \in (35°, 75°)$, and therefore, they are well fit by the DH-PSF method. Molecules 3 and 4 show excellent agreement between the orientations estimated by the DH-PSF and the orientations estimated from defocused image template matching. Molecules 5 and 6 are not inclined much at all ($\theta > 75°$), and therefore, the DH-PSF method does not yield orientation estimates that agree as well. Small values of $|LA|$ lead to degeneracies in the estimated parameters for these molecules. However, for the purpose of correcting dipole-induced mislocalizations, this fact is not of much importance, because noninclined molecules have negligible shifts (Fig. S5).

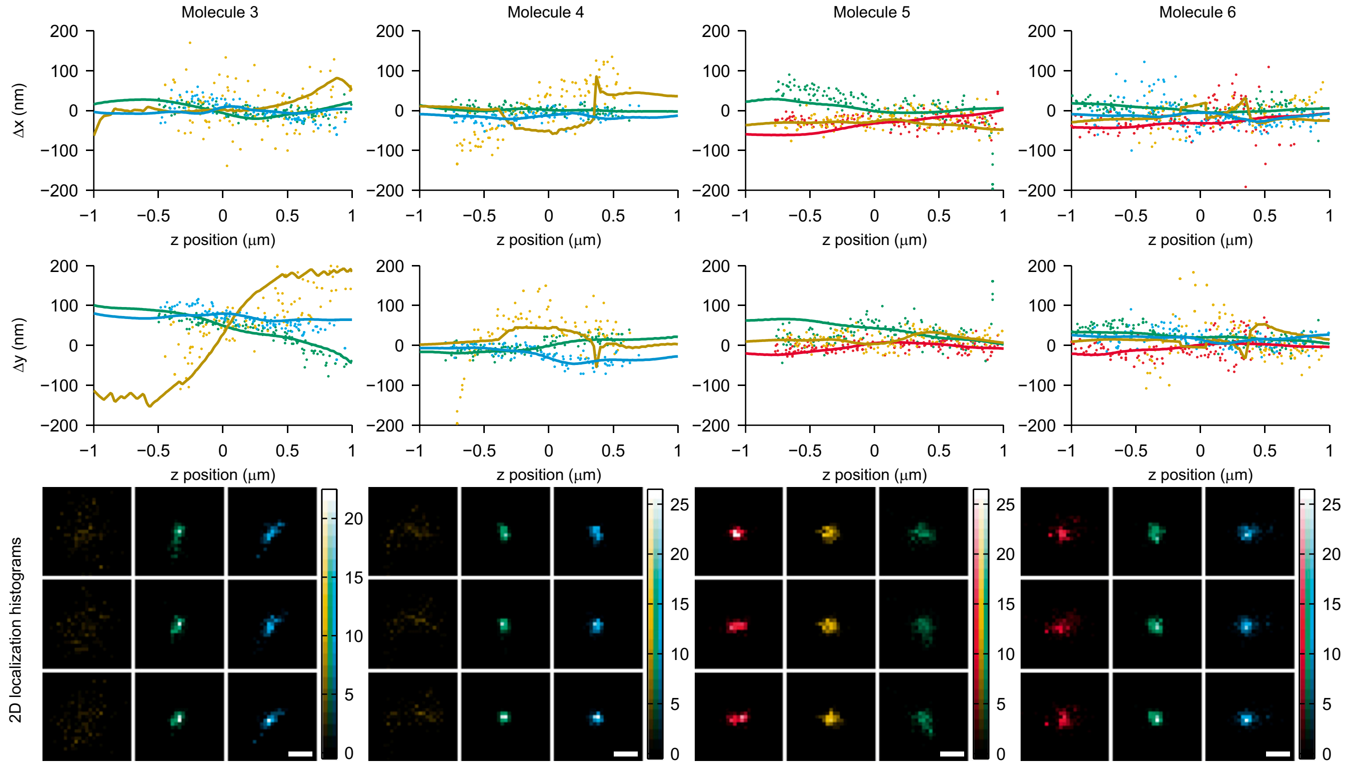

Fig. S5. Measured and predicted (Δ*x*,Δ*y*) caused by dipole effect for molecules 3–6. Measured (scatter points) Δ*x* (*Top*) and Δ*y* (*Middle*) vs. *z* for each molecule (each column), with overlay (solid line) of predicted shift based on the mean extracted orientation. Highly inclined molecules (molecules 3 and 4; columns 1 and 2) generally experience larger dipole shifts than slightly inclined molecules (molecules 5 and 6; columns 3 and 4). For molecules 3–5, one mask orientation/polarization combination did not produce meaningful localizations because of low signal and/or high *LA* (omitted channels). Images in *Bottom* show 2D histograms of uncorrected ($x_{apparent}$,$y_{apparent}$) localizations (*Top*), corrected localizations based on individual estimations of (θ, ϕ) (*Middle*), and corrected localizations based on average estimate of (θ, ϕ) (*Bottom*). Histograms for cases with significant directional shifts (green channel of molecules 3 and 4; blue channel of molecule 4) become more concentrated and less elongated when corrected. Bin size, 15 nm. (Scale bars: 100 nm.) Color code is the same as in Figs. 3 and 4.

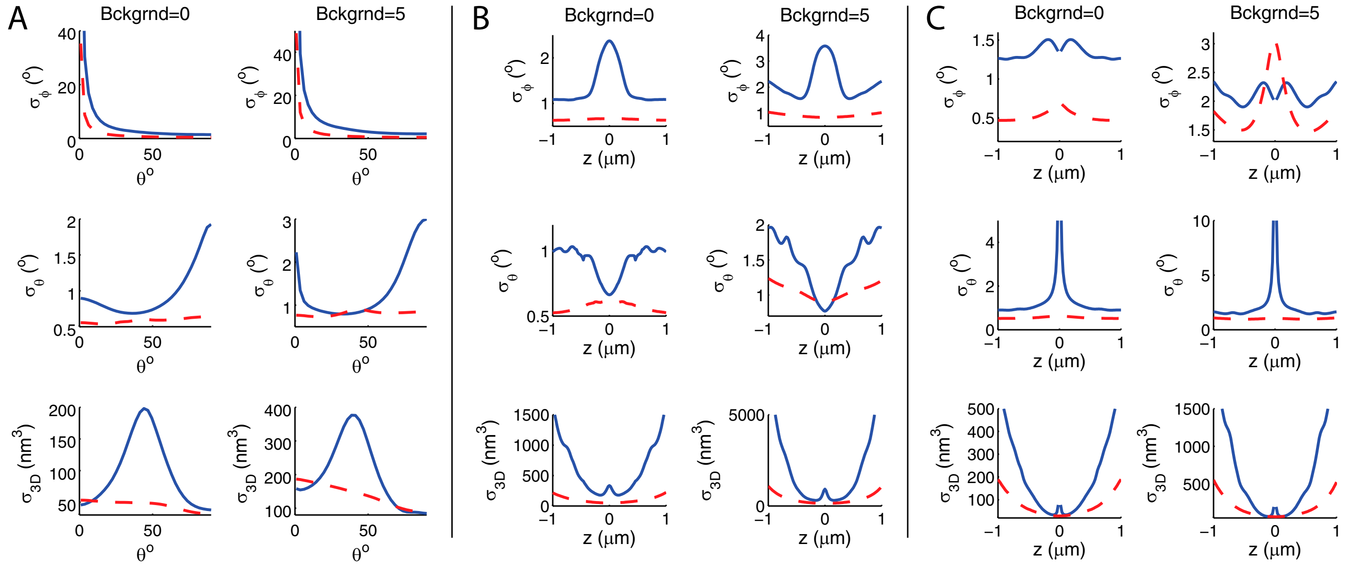

Fig. S6. Lower bound of the precision (SD) for estimating the azimuthal angle (σ_ϕ), polar angle (σ_θ), and 3D position (σ_{3D}) based on CRLB calculations. Blue solid curves represent the standard PSF case, and dashed red curves represent the DH case. (*A*) Precisions as functions of θ without background (*Left*) and with a background of five photons per pixel (*Right*). ϕ = 45°, the standard PSF case is defocused by 100 nm, and the DH case is in focus. (*B* and *C*) Precisions as functions of defocus (*z*) without background (*Left*) and with a background of five photons per pixel (*Right*) for a dipole with (*B*) orientation (θ, ϕ) = (45°, 45°) and (*C*) orientation (θ, ϕ) = (90°, 90°).

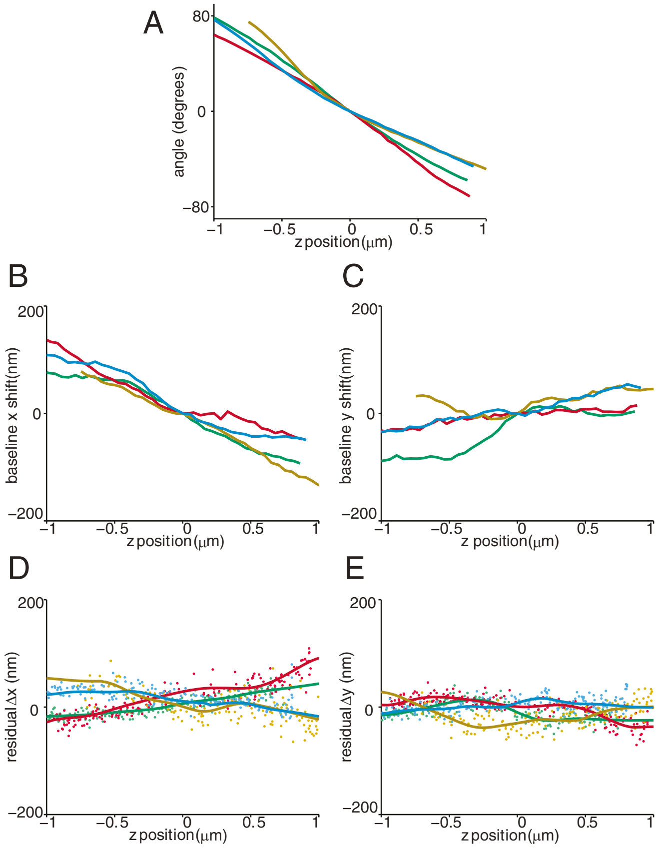

Fig. S7. Calibration curves used in SM fitting. Color code is same as in Figs. 3 and 4. (*A*) Angle made by two DH-PSF lobes vs. *z* as measured from a fluorescent bead. Different optical paths and different lateral offsets of the phase mask make for different curves in the four channels. (*B* and *C*) Baseline *x* and *y* vs. *z* curves. Nonidealities such as sample tilt, aberrations, and lateral mask offset cause a nonzero lateral shift in the PSF, even for an isotropic emitter, which must be subtracted out. (*D* and *E*) Residual lateral shifts vs. *z*. Because the fiducial beads are embedded in a slightly different medium, application of just the bead calibration curves leaves some residual shift for SMs that is caused by factors other than dipole orientation. Residual lateral shift calibration curves are calculated by subtracting the predicted shifts from the apparent shifts of two calibration molecules (*SI Text*).

Table S1. Average photons detected above background in each channel for each molecule

Molecule no.	Green	Red	Gold	Blue	Total
1	1,100	700	510	1,300	3,610
2	1,900	2,600	2,100	2,200	8,800
3	2,200	240	820	2,600	5,860
4	2,000	1,400	1,200	1,900	6,500
5	1,300	2,100	1,800	1,300	6,500
6	1,600	930	650	1,100	4,280
Mean total					5,925

Calculated by integrating all photons within a 15 × 15-pixel box containing the molecule and subtracting the average background photons contained in this area. Average background for each molecule was determined by measuring the background in a nearby hand-designated region (~9 photons/pixel per frame average across all molecules).

Table S2. **σ_a at 2-µm depth range for molecules 1 and 2 compared to localization precision**

	Green		Red		Gold		Blue	
	σ_a (nm)	σ_a/precision	σ_a (nm)	σ_a/precision	σ_a (nm)	σ_a/precision	σ_a (nm)	σ_a/precision
Molecule 1								
Uncorrected	54	3	—	—	116	4.1	36	1.4
Individually corrected	35	1.9	—	—	55	2	37	1.5
Mean corrected	24	1.3	—	—	34	1.2	36	1.4
Precision	18	—	—	—	28	—	25	—
Molecule 2								
Uncorrected	48	1.9	35	2.1	26	0.96	—	—
Individually corrected	30	1.2	21	1.2	28	1	—	—
Mean corrected	28	1.1	18	1.1	27	1	—	—
Precision	25	—	17	—	27	—	—	—

Precision was calculated by binning localizations into 100-nm *z* bins and taking the SD along **a** in each bin. These values were then averaged across all bins within the center ~1 µm of the *z* range. Our corrections show significant improvement in cases that have σ_a ~2× larger than precision or worse (molecule 1, green and gold channels; molecule 2, green and red channels).

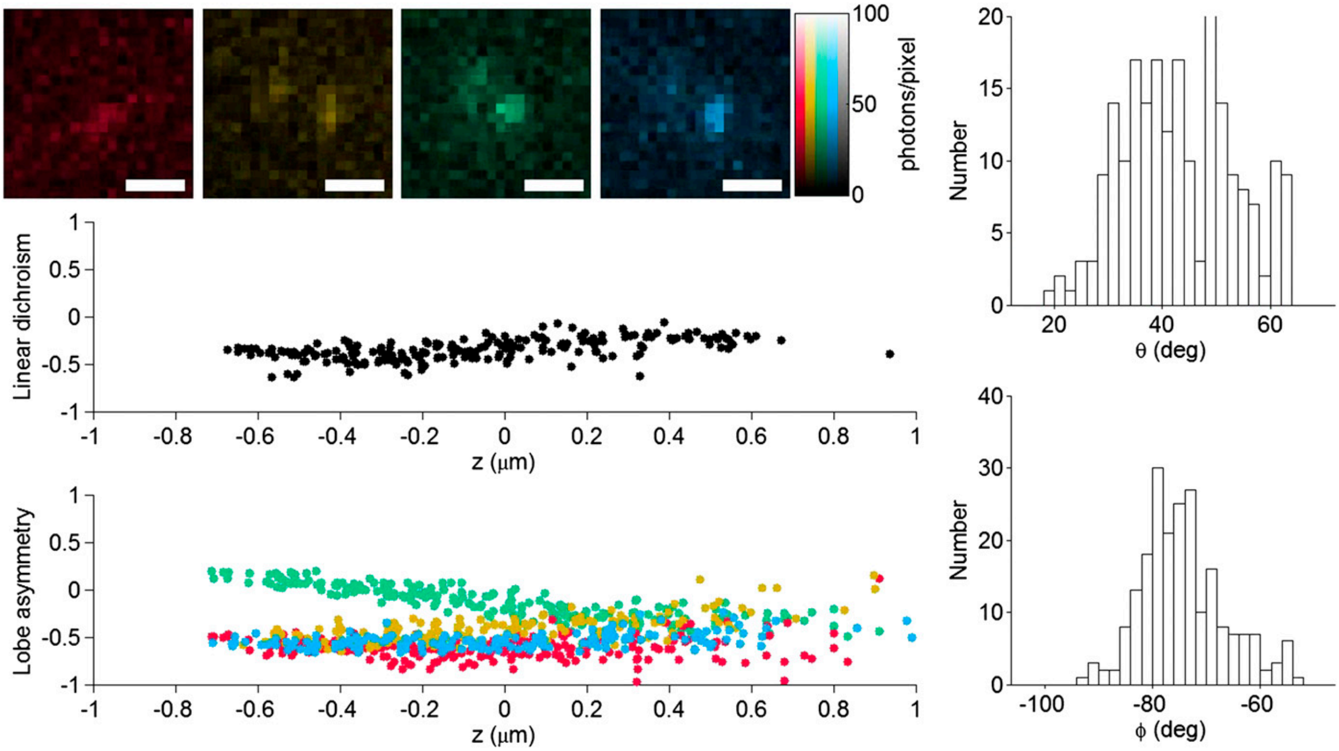

Movie S1. DH-PSF–based molecular orientation measurements of molecule 1 over two axial (*z*) scans. The raw DH microscope images from each of the four measurement channels (red, gold, green, and blue) are shown in the upper left. Linear dichroism (middle left) and lobe asymmetry (bottom left) are depicted as scatter points because they are measured during the scans. Finally, histograms of the calculated polar and azimuthal orientation of molecule 1 are plotted at right. The final frames of the movie show *LD* and *LA* (as solid lines) for the mean orientation measured for molecule 1 (center of the Gaussian fits at right).

Movie S1